Journal of Materiomics 11 (2025) 100905

Contents lists available at ScienceDirect

Journal of Materiomics

journal homepage: www.journals.elsevier.com/journal-of-materiomics/

Research paper

Dual-phase ceramics based on multi-cation boride and carbide: Investigations at the nanoscale

Steven M. Smith II [a], Nicola Gilli [b], William G. Fahrenholtz [a], Gregory E. Hilmas [a], Sandra García-González [c], Emilio Jiménez-Piqué [c, d], Stefano Curtarolo [e, f], Laura Silvestroni [g, *]

[a] University of Science and Technology, Materials Science and Engineering Department, Rolla, MO, USA
[b] CNR-IMM, Institute of Microelectronics and Microsystems, Bologna, Italy
[c] Dept. of Materials Science and Eng., EEBE, Univ. Politècnica de Catalunya-BarcelonaTECH., Barcelona, Spain
[d] Barcelona Research Center in Multiscale Science and Eng. - Univ. Politècnica de Catalunya-BarcelonaTECH., Barcelona, Spain
[e] Center for Extreme Materials, Duke University, Durham, NC, USA
[f] Department of Mechanical Engineering and Materials Science, Duke University, NC, USA
[g] CNR-ISSMC, Institute of Science, Technology and Sustainability for Ceramic Materials, Faenza, Italy

ARTICLE INFO

Article history:
Received 27 February 2024
Received in revised form
16 May 2024
Accepted 10 June 2024
Available online 26 June 2024

Keywords:
High entropy boride
High entropy carbide
Segregation
Nanoindentation
TEM

ABSTRACT

A dual phase boride and carbide ceramic with the nominal composition $(Ti_{0.2}Zr_{0.2}Hf_{0.2}Nb_{0.2}Ta_{0.2})B_2$ and $(Ti_{0.2}Zr_{0.2}Hf_{0.2}Nb_{0.2}Ta_{0.2})C$ was prepared by reactive synthesis and consolidated by spark plasma sintering. The resulting microstructure contained about 30% (in volume) boride and 70% carbide. Compositional inhomogeneities were observed within single grains that had core-shell structures and preferential accumulation of specific metals in the boride or carbide phases. Specifically, Ti and Nb had higher concentrations in the boride, whereas Hf and Ta in the carbide. The Zr concentration was relatively equally distributed in the two phases. The dual phase ceramic had additional, distinctive features including nanosized inclusions, possibly related to local miscibility gaps and supersaturation, linear defects, and strain due to adjustment of the crystal structure. As a consequence, the fracture mode was transgranular with the crack path deviated by these nanometric microstructure alterations. Nanoindentation under 5 mN measured higher hardness and modulus for the boride, 30 GPa and 525 GPa, as compared to the carbide phase, 22 GPa and 425 GPa, due to a higher concentration of dislocation tangles and strains deriving from the introduction of metals with different sizes (and properties) in a less compliant hexagonal lattice.

1. Introduction

The simultaneous combination of several metals within the same oxide, carbide, or boride structure results in superior hardness, strength, and oxidation resistance compared to the conventional single components ceramic [1–5]. These compounds are generally referred to as high entropy materials (HEMs) and are assumed to consist of solid solutions where elements are randomly distributed, rather than ordered or intermetallic phases. The high-entropy effect increases the thermodynamic stability of HEMs through the higher entropy of mixing [1,6–8].

Borides, carbides, nitrides, and oxides (and combinations thereof) of transition metals are suitable for extreme environments, such as those encountered in energy management and aerospace applications, due to their high points exceeding 3000 °C and appealing combinations of thermal and mechanical properties [9–12]. In this respect, high entropy borides (HEBs) and high entropy carbides (HECs) are gaining attention due to their potential for improved performance [4,13]. The first studies on single HEB and HEC ceramics revealed some issues in fabrication, since extreme processing conditions are needed to homogenize the solid solutions and densify the resulting ceramics. However, these same studies also achieved some promising results. For example, homogeneous cation distribution at the micro and nano/atomic level was achieved in HECs produced by two-step spark plasma sintering

* Corresponding author.
E-mail address: laura.silvestroni@cnr.it (L. Silvestroni).
Peer review under responsibility of The Chinese Ceramic Society.

https://doi.org/10.1016/j.jmat.2024.06.002

(SPS) with a holding time of 7 min at 2300 °C, which resulted in grain sizes in the range of 5–25 μm [14]. On the other hand, cation inhomogeneities, particularly Nb segregation, were observed in equimolar HEB processed by a similar two-step SPS process with a peak temperature of 2100 °C [15,16]. Segregation of Nb was possibly driven by the low solubility of NbB_2 in the other transition metal borides or slow diffusion of Nb during synthesis and densification.

HEB ceramics exhibit higher hardness than expected based on the hardness values of the individual constituent diboride ceramics, which has been attributed to disorder associated with the presence of multiple transition metals and solid solution hardening [16,17]. In addition, the room-temperature strength of single-phase HEC ceramics was retained up to 1800 °C, compared to loss of strength at lower temperatures for individual carbides [18]. Strength retention of HECs was attributed to decreased dislocation density in the HECs. Similarly, exceptional values of strength at elevated temperature were recently measured for a single-phase HEB [19], remaining above 750 MPa up to 2000 °C before deforming at higher temperatures [20]. Strength retention was also observed for simpler boride solid solutions based on $(Zr,W)B_2$ [21,22] which was attributed to the core-shell structure of the grains and accumulation of dislocations at core-shell interfaces. HE ceramics may have a higher resistance to dislocation movement compared to single-metal diboride compositions or simpler solid solutions due to lattice distortion and solid solution strengthening effects. Different strengthening mechanisms can be exploited to obtain high strength and hardness in multiphase materials, the most common ones are phase transformation, solid-solution, dislocation, grain-boundary, precipitation hardening, and load transfer *via* the introduction of strong phases. Of these, load transfer and precipitation strengthening are considered to be the two most effective strengthening mechanisms [23].

A natural progression from these investigations was the combination of HEB and HEC into dual phase HE-UHTCs [24–27]. Thermodynamic analysis further pinpointed fundamental relations that explained preferential segregation of specific metals into either the boride or carbide phase resulting in tunable properties that can be controlled by changing the phase fraction and microstructure [28–30]. In addition, hierarchical architectures, involving nanoprecipitates in micron-sized grains, lattice distortion, and solid solution strengthening effects, may lead to further increases in strength at elevated temperatures in HE ceramics, similar to what has been observed for HE alloys [23].

The present paper reports the fabrication, nano-structure, and local properties of a dual HEB-HEC material supported by TEM analyses and nanoindentation. The innovative aspect of this work relies in the correlation of microstructural features observed at the nano-scale length to the actual local mechanical properties that explain the higher hardness of the HEB as compared to the HEC.

2. Experimental section

2.1. Materials preparation

The HEB-HEC ceramic was produced using the sequential method outlined by Smith et al. [31] Hafnium oxide (HfO_2, 99%, ~325 mesh, Alfa Aesar), niobium oxide (Nb_2O_5, 99.5%, ~100 mesh, Alfa Aesar), tantalum oxide (Ta_2O_5, 99.8%, 1–5 μm, Atlantic Equipment Engineers), titanium oxide (TiO_2, 99.9%, 32 nm APS, Alfa Aesar), zirconium oxide (ZrO_2, 99%, 5 μm, Sigma-Aldrich), and carbon black (C, BP1100, Cabot) were used to first react a high-entropy carbide. The oxides and carbon were batched to produce $(Ti_{0.22}Zr_{0.11}Hf_{0.22}Nb_{0.22}Ta_{0.22})C$. Note that the zirconium content was reduced in the HEC synthesis to account for the production of ZrC during the second reaction, as described below. An excess of 0.75% (in mass) C was added to compensate for carbon loss during the reaction. The batched powders were mixed by dry high energy ball milling (SPEX D8000, SPEX CertiPrep) using WC jars and 6 mm WC milling media for two 1 h cycles with a 30-min cooling period between cycles. A media to powder mass ratio of 7.5 was used to mill a 20 g batch of powder. The milled powders were passed through a US 80 mesh sieve and then pressed into a 25 mm disk to promote powder contact during the reaction and prevent powder loss. The powder was reacted in a graphite element furnace (HP50-7010G, Thermal Technology) at 1600 °C under vacuum (≤13 Pa) for 2.5 h. After reaction, the powder was allowed to cool under vacuum and the resulting powder was passed through a US 100-mesh sieve.

The HEB phase was formed by reacting part of the HEC powder with boron carbide (B_4C, 96.8%, 0.6–1.2 μm, HC Starck) and zirconium hydride (ZrH_2, 95.5%, 21.1 μm, Chemadyne). The powders were mixed by wet ball milling in acetone with 6 mm WC milling media for 24 h in a low density polyethylene bottle. A media to powder mass ratio of 7.5 was used. ZrH_2 was added to remove free carbon produced when the HEB is formed by Eqn 1 and produces ZrC according to Eqn 2 that then dissolves into the HEC phase.

$$HEC + B_4C \rightarrow HEB + C \quad (1)$$

$$C + ZrH_2 \rightarrow ZrC + H_2 \quad (2)$$

The total Zr content in the system was balanced by adjusting the starting carbide composition that was indeed Zr-deficient as compared to an equimolar content.

The milled powder was dried by rotary evaporation (Rotavapor R-124, Buchi) and passed through a US 80-mesh sieve and was pressed into a 25 mm disk. The powder was reacted a second time in a graphite element furnace for 1650 °C for 2.5 h under vacuum. The resulting powder was passed through a US 100 mesh sieve.

The reacted powder mixture was densified by spark plasma sintering (SPS, DCS10, Thermal Technology) in a 20 mm graphite die lined with graphite foil. The die was first loaded to 15 MPa under vacuum (≤13 Pa), heated at 100 °C/min to 1650 °C, and held

Table 1
Nominal composition, nominal theoretical density (ρ^N_{th}) and recalculated from the actual composition determined by EDS (ρ^*_{th}), lattice parameters from XRD, lattice parameters from electron diffraction (ED), and mean grain size of HEB and HEC.

Sample	Nominal composition	ρ^N_{th} (g·cm^{-3})	ρ^*_{th} (g·cm^{-3})	Lattice parameters from XRD (nm)	Lattice parameters from ED (nm)	Grain size (μm)
HEB	$(Ti_{0.2}Zr_{0.2}Hf_{0.2}Nb_{0.2}Ta_{0.2})B_2$	8.24	6.59	$a = 0.3115(4)$ $c = 0.3410(7)$	$a = 0.317(5)$ $c = 0.340(0)$	1.1 ± 0.5
HEC	$(Ti_{0.2}Zr_{0.2}Hf_{0.2}Nb_{0.2}Ta_{0.2})C$	9.48	8.64	$a = 0.4579(3)$	$a = 0.460(0)$	1.2 ± 0.5

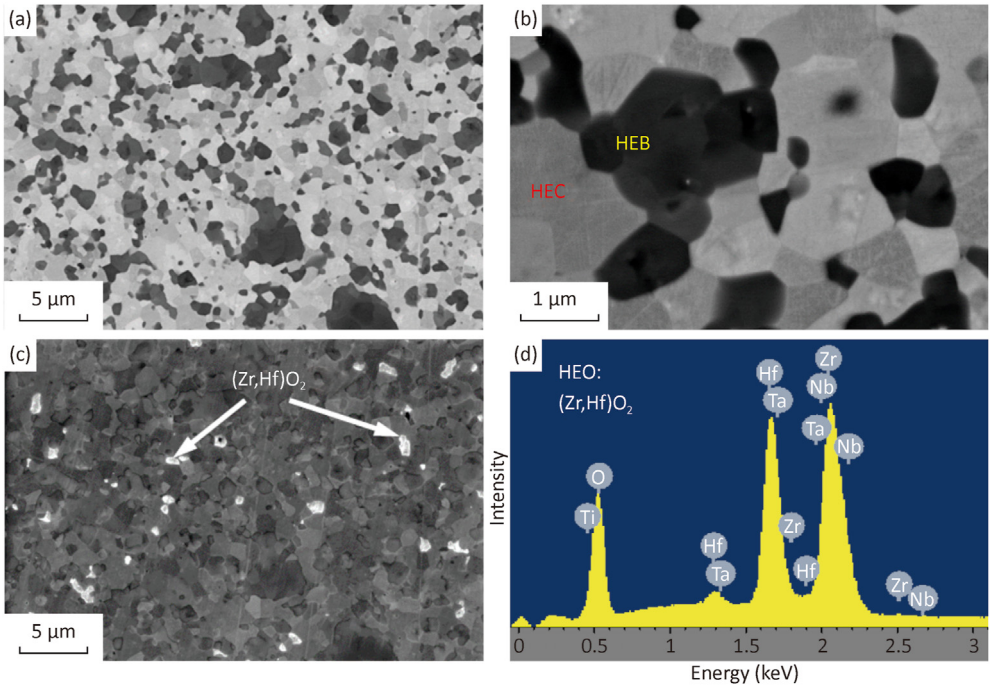

Fig. 1. SEM images showing (a) a microstructure overview, (b) high magnification of the ceramic highlighting inhomogeneous contrast across the grains, (c) residuals of oxide phase (bright phase) with corresponding EDS in (d).

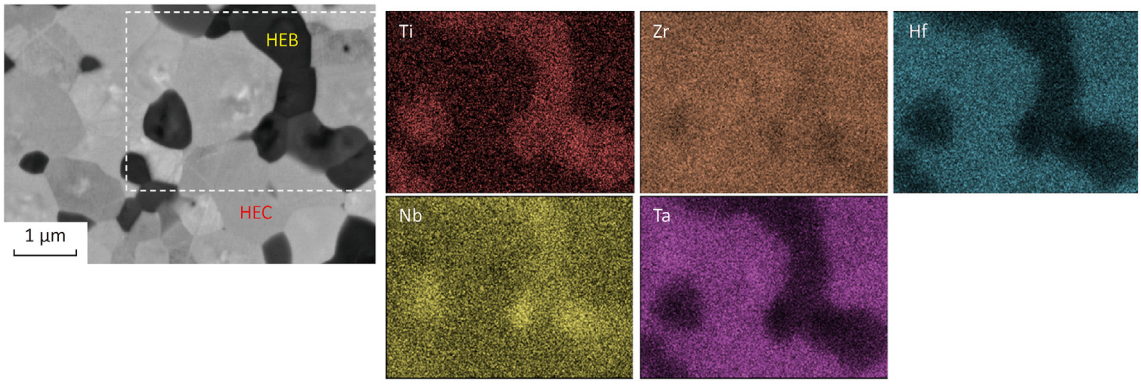

Fig. 2. SEM images showing segregation of metals with higher concentrations of Ti and Nb in the HEB, higher Hf and Ta concentrations in the HEC, and nominally homogeneous distribution of Zr between the two phases.

for 5 min. Then, the pressure was increased to 50 MPa and the die was heated to 2000 °C at 150 °C/min and held at temperature for 10 min. The die was cooled at a controlled rate of 50 °C/min to 1200 °C and then allowed to cool at the natural furnace rate under flowing Ar gas.

2.2. Characterization

The nominal theoretical density was first calculated based on the batched composition, ρ^{N}_{th}, and then corrected according to the actual composition measured by energy dispersive X-ray spectroscopy (EDS), ρ^{*}_{th}. The relative density was the ratio between the one measured by Archimedes' method and ρ^{*}_{th}, Table 1. The lattice parameters were determined by Rietveld refinement of the X-ray diffraction (XRD, X-Pert MPD, Philips) data and also by electron diffraction (ED).

The sintered ceramics were sectioned and polished to inspect the microstructure. Field emission scanning electron microscopy (FE-SEM, Carl Zeiss Sigma NTS Gmbh, Oberkochen, DE) coupled with EDS (INCA Energy 300, Oxford instruments, UK) was used to analyze the microstructure and composition on polished and fractured surfaces. Lamella for transmission electron microscopy (TEM) were prepared by focused-ion beam (FIB, ZEISS CrossBeam 340 FIB/EBL, Oberkochen, DE). Local phase analysis was carried out using a TEM (FEI Tecnai F20 ST TEM, Hillsboro, USA) with a nominal accelerating voltage of 200 kV and equipped with EDS (Oxford Instruments, Abingdon, UK). Electron diffraction patterns were resolved through the commercial software JEMS (Java Electron Microscopy Software, P. Stadelmann, Switzerland) and the Strain++ software was used to obtain graphic phase analysis on HRTEM images.

The micro-mechanical properties of the sintered ceramics were

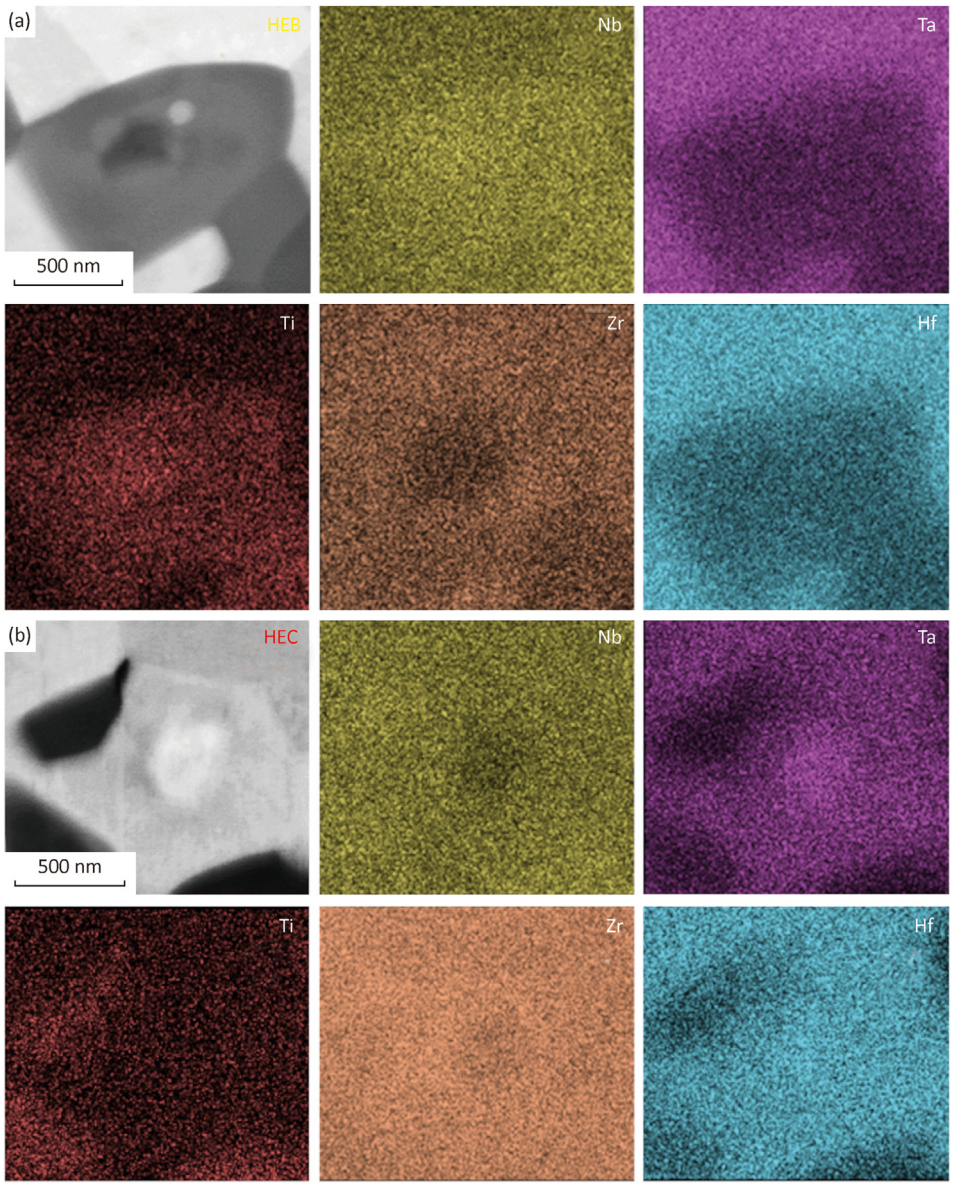

Fig. 3. SEM images showing magnified views of (a) boride and (b) carbide grains with corresponding EDS elemental mapping showing core-shell structures within individual grains.

Table 2
Composition of HEB and HEC as estimated by SEM-EDS in the various core-shell regions.

Position	Mole fraction (%)				
	Ti	Zr	Hf	Nb	Ta
Boride-core	25	29	8	32	6
Boride-shell	21	43	8	20	8
Carbide-core	7	45	17	13	18
Carbide-shell	7	47	14	14	18

measured by nanoindentation (KLA iMicro nanoindenter, KLA Corp., USA) equipped with a Berkovich diamond tip with its function area calibrated against fused silica. A map of 50 × 50 indentations was performed at a load of 5 mN resulting in an approximate penetration depth of 90 nm with a 3 μm spacing between the indentations. The indenter was continuously loaded up to the peak load with a strain rate of $\frac{\dot{h}}{h} = 0.05s^{-1}$ and immediately unloaded with no holding time. Hardness and elastic modulus were calculated using Oliver and Pharr's method [32]. A Poisson's ratio equal to 0.11 was set based on literature data of high entropy ceramics with the same nominal composition [33].

3. Results and discussion

3.1. Microstructural details

The bulk density was 8.06 g/cm^3, which was significantly different from the expected theoretical density of 9.19 g/cm^3 that was based on individual HEB and HEC phases with equal amounts of the constituent metals. This disparity between the measured bulk and estimated theoretical densities was due to preferential segregation of metals to either the HEB or HEC, as described below.

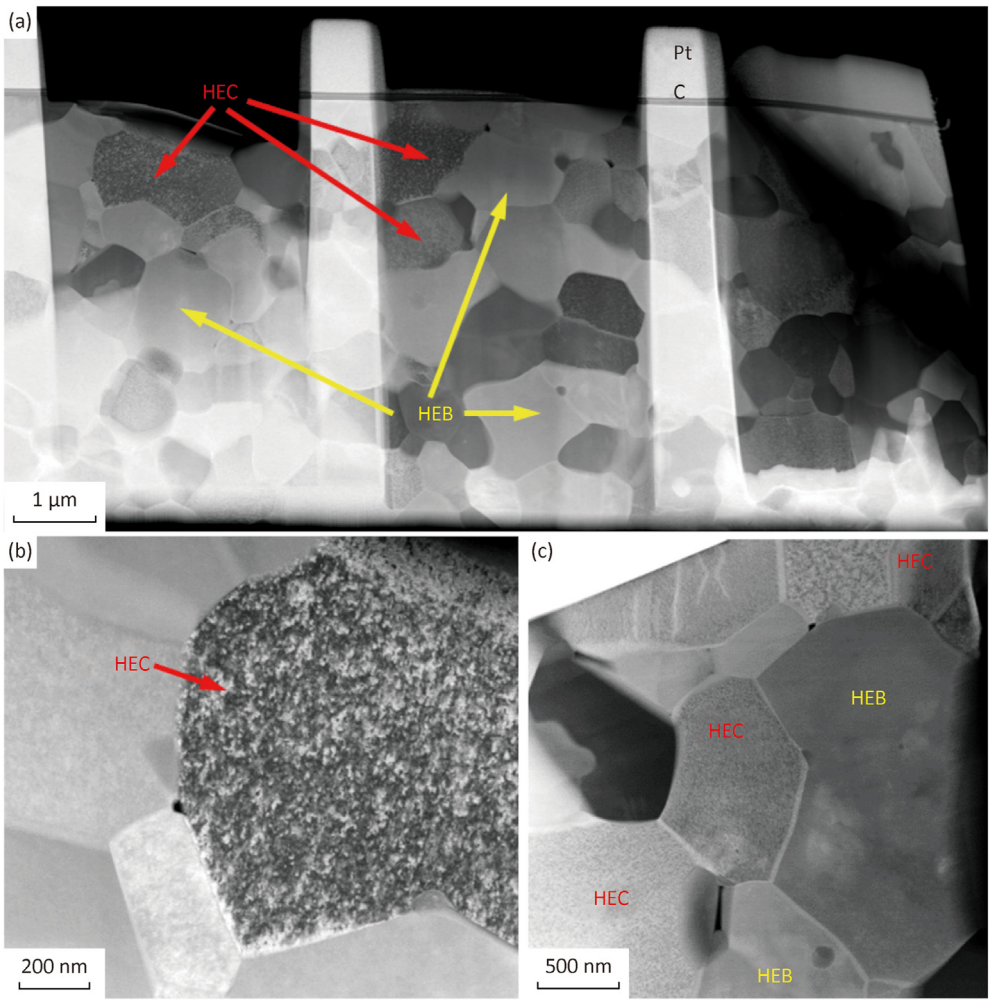

Fig. 4. TEM images showing (a) an overview of the lamella obtained by FIB, (b) "orange peel" surface finishing in HEC grain and (c) contrast shadowing due to composition alteration in the HEB-HEC grains.

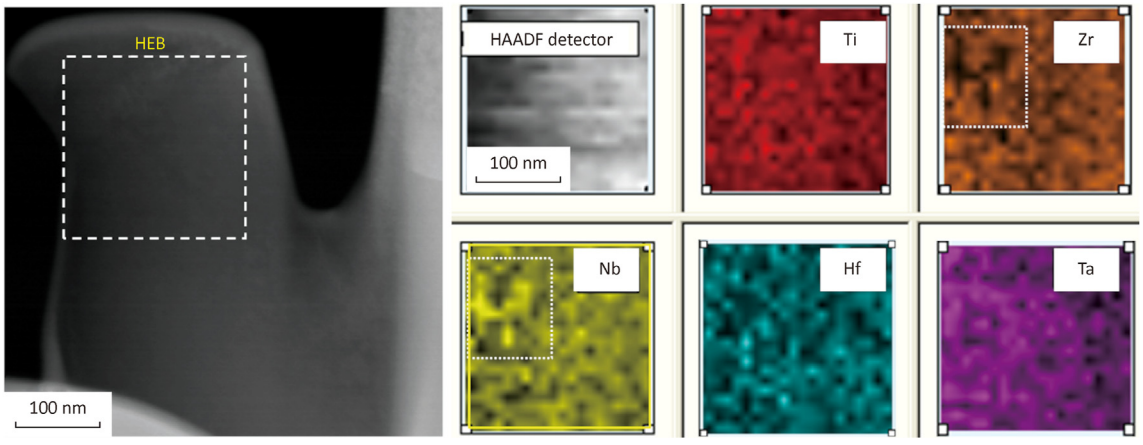

Fig. 5. High Resolution S/TEM EDS elemental mapping on a HEB grain showing Nb enrichment and Zr depletion.

The lattice parameters are summarized in Table 1. The lattice parameters for the HEB and HEC phases were also estimated from ED patterns and were in relatively good agreement with the lattice parameter determined by XRD, Table 1.

An overview on the microstructure of the sintered ceramic is reported in Fig. 1a. The residual porosity was negligible, confirming that the ceramic was fully dense. Using backscattered electron imaging, a uniform distribution of the boride grains with dark

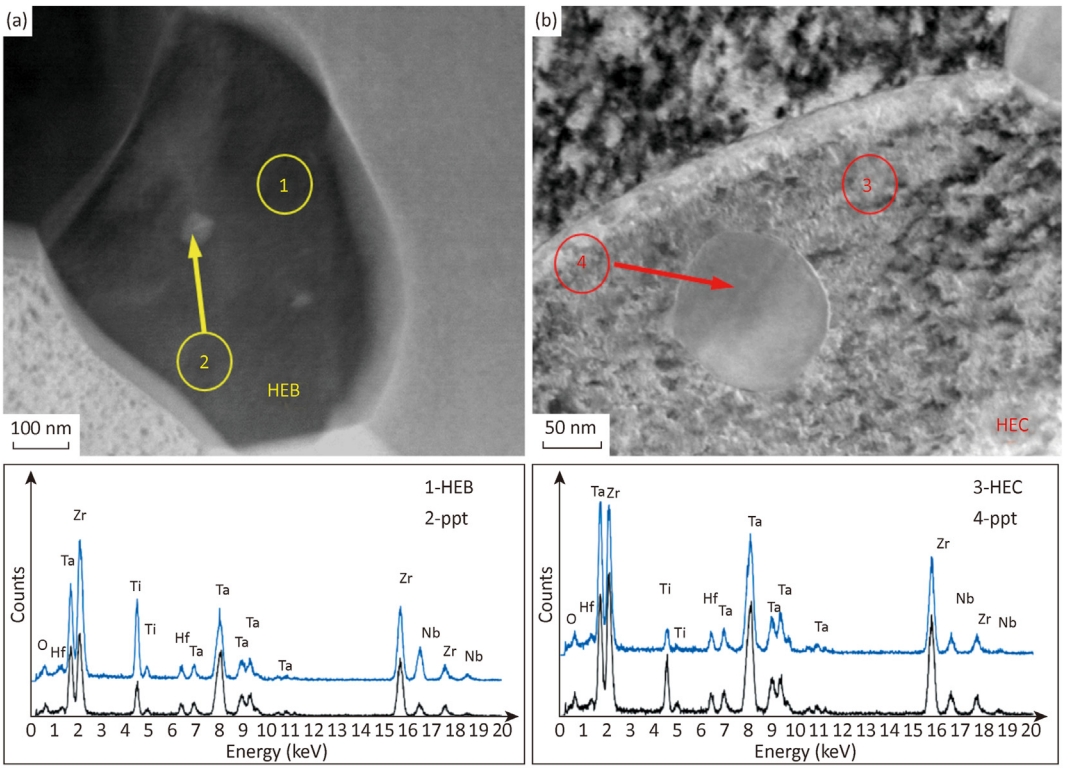

	Mole fraction				
Position	Ti	Zr	Hf	Nb	Ta
1-HEB shell	18	39	18	10	15
2-ppt	16	44	14	12	14
3-HEC shell	6	42	17	10	25
4-ppt	12	42	15	1	21

Fig. 6. TEM images showing nano-precipitates (ppt) in both (a) HEB and (b) HEC grains with corresponding EDS spectra where compositional differences are highlighted in the table below.

contrast and carbide grains with bright contrast was assessed. The relative amounts of the HEB was 30% (in volume) while the HEC was about 70% (in volume), which is close to the target composition. The mean grain size of the HEB was (1.1 ± 0.5) μm and (1.2 ± 0.5) μm for the HEC, similar to previous reports [31].

Higher magnification images revealed different contrast shades within the individual grains, which were captured with different brightness and contrast conditions to highlight the boride or carbide phases, Fig. 1b. Color inhomogeneities were ascribed to compositional differences, which was confirmed by EDS mapping that showed preferential segregation of certain metals in the boride or carbide phases. WC contamination from the milling media was negligible in the final ceramic. Using the *In lens* detector, about 3% (in volume) of residual oxide phase was observed, Fig. 1c. The oxide contained mainly Zr and Hf with a composition close to $(Zr_{0.66}Hf_{0.33})O_2$. Only trace amounts of Ti, Nb and Ta were detected in the oxide phase, Fig. 1d.

Magnified portions of the ceramic, highlighting compositional inhomogeneities, are shown in Figs. 2 and 3. SEM images are accompanied by corresponding EDS elemental maps. From Fig. 2, Ti and Nb appear to preferentially segregate to the boride, while Hf and Ta preferentially segregate to the carbide, which is in agreement with thermodynamic predictions based on the standard Gibbs' free energy of formation for the borides and carbides of the individual transition metals [30]. In contrast to the segregating metals, Zr is homogeneously distributed in the two phases. The overall Zr content was higher than the other metals due to the processing route that used additional ZrH_2 to react with excess carbon to produce ZrC, thus increasing the total amount of Zr in the system [31].

Focusing on an individual boride grain, Fig. 3a, the cores were rich in Ti and Nb, but depleted in Zr. Both Hf and Ta had lower concentrations, but were homogeneously distributed across the grain volume. Within an individual carbide grain, Fig. 3b, the core was rich in Hf and Ta, but depleted in Zr and Nb. Although distributed homogenously across the carbide grain volume, Ti had a lower concentration. The most reliable compositions of core and shell in HEB and HEC phases, as measured by SEM-EDS, are reported in Table 2.

Inspection by TEM confirmed that the ceramics were fully dense, with contrasts opposite as compared to SEM imaging. The boride grains were brighter with a smooth surface, while the carbide had darker contrast and a rougher orange peel like texture, Fig. 4a and b. This typical appearance of the carbide, which is also observed in nominally pure carbides, is possibly due to vacancies [34] or higher sensitivity to ion damage and implantation [35] than the boride. Contrast variations due to composition changes were partially blurred by thickness effects; however, when the specimen

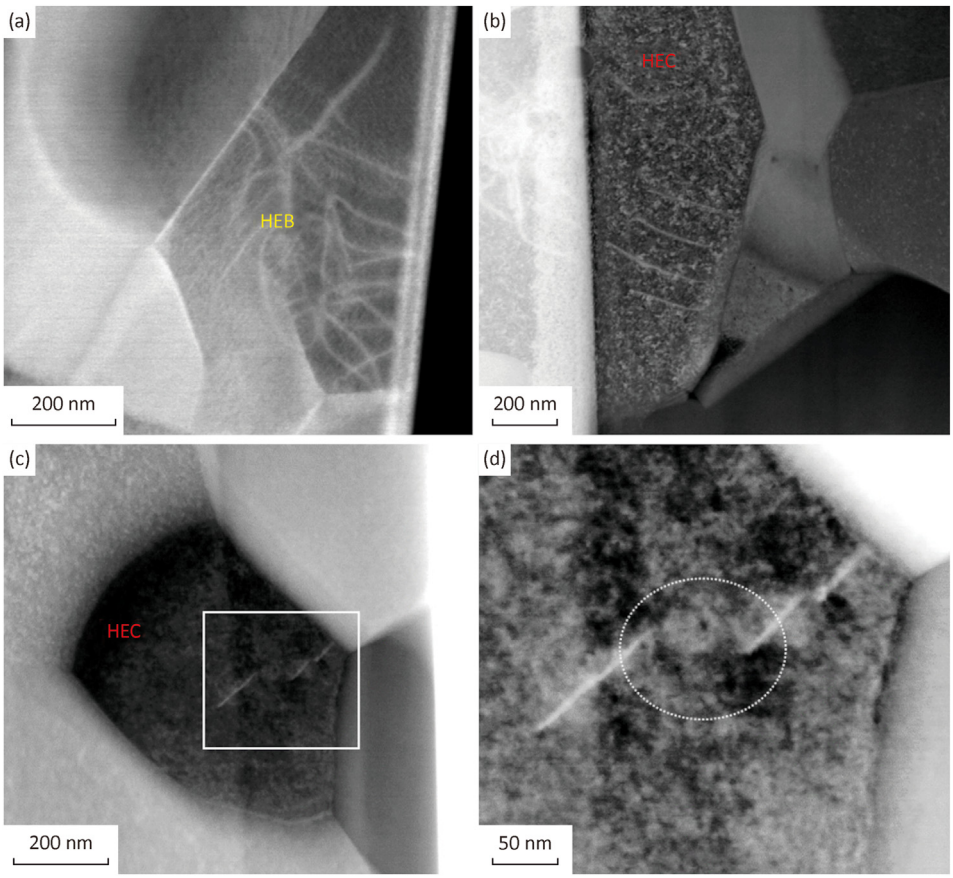

Fig. 7. TEM images showing dislocation activity in (a) HEB and (b) HEC grains and deflection across nano-sized inclusions in (c)–(d).

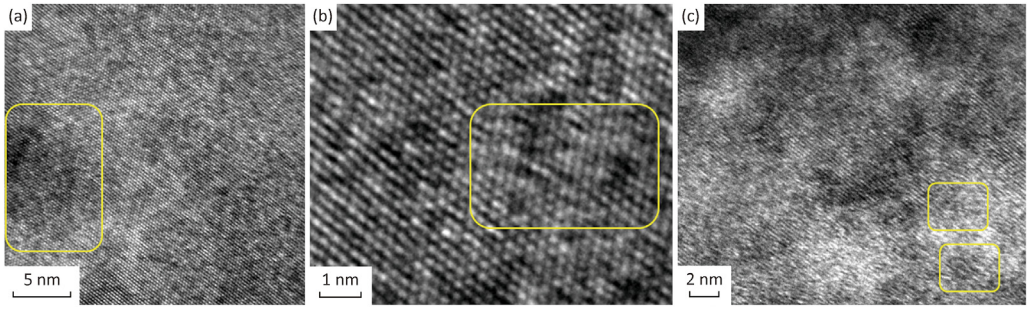

Fig. 8. HR-TEM pictures of a HEB grain from [001] zone axis projection showing, (a) strain accumulation due to compositional disorder, (b) Frank partial dislocation, and (c) coffee bean strained zones.

was thin enough, contrast inhomogeneities were observed in both types of grains, Fig. 4c. Elemental profile linescans were run across grain boundaries, but no particular element segregation was observed, differently to what reported for high entropy alloys [36], predicted in medium and high entropy carbides [37] and observed in W– and W–Mo-containing high-entropy borides [38].

A detailed EDS mapping on boride grains further revealed metal segregation. For example, Fig. 5 shows the chemical composition of a boride grain that is rich in Nb, but relatively poor in Zr.

Rounded inclusions were observed trapped within both boride and carbide grains, both in SEM and TEM Fig. 6. These inclusions could be related to local miscibility gaps [39] and super-saturation of specific metals in the grains. The inclusions were rich in Zr when encapsulated in HEB grains, or rich in Ti and poor in Nb when encapsulated in HEC grains. The nature of these inclusions, whether they were carbide, boride, oxide, or spurious phase, is unknown; however, given their smooth appearance, they could be borides. Very few dislocations were observed. When they were found, they had brighter contrast and, for some cases, were found to be pinned by the rounded inclusions, Fig. 7d.

High resolution imaging in both boride and carbide grains revealed systematic localized strains that could be related to local chemistry variations, Fig. 8a. Furthermore, Frank partial dislocation, where one plane of atoms was missing after being consumed by the surrounding lattice, were frequently observed, Fig. 8b. Another feature typical of HR-imaging was the presence of sparsely distributed, faint “coffee bean” like contrast, Fig. 8c. Coffee bean contrasts generally arises due to strain fields associated with lattice

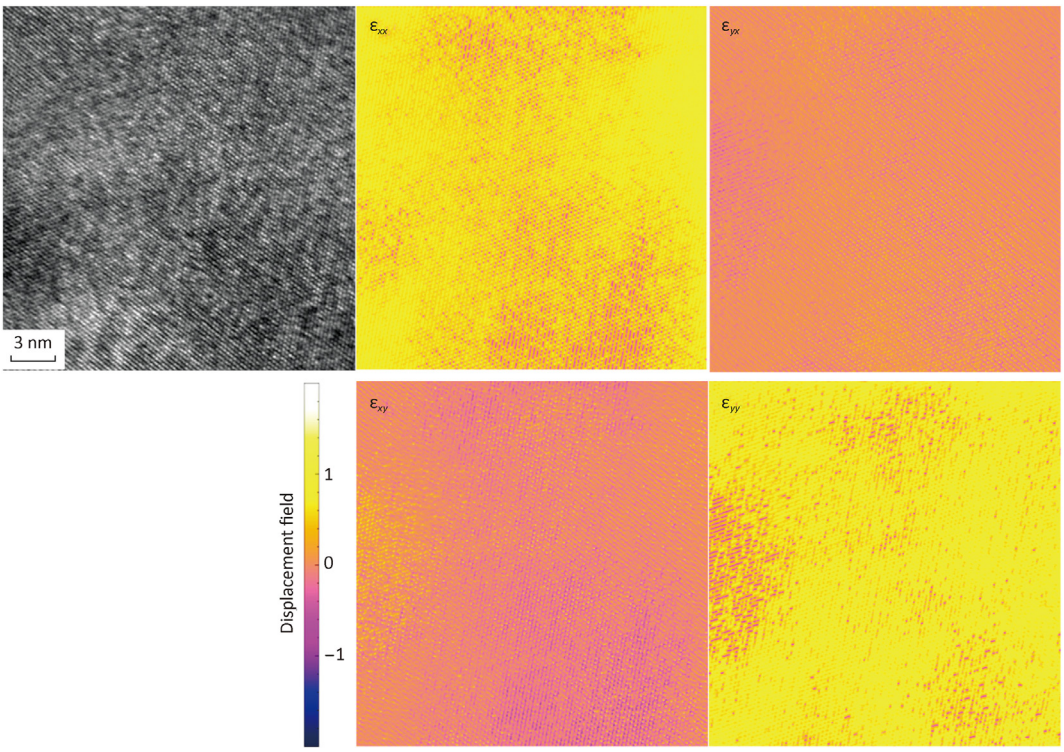

Fig. 9. Reference HR-TEM image of a HEB grain, zone axis [001], and corresponding displacement field. The *x*-axis is parallel to the 100 direction and the *y*-axis is parallel to the 010 direction of the reference lattice. The displacement field is given as fractions of unit cell vectors, where purple = −1 and yellow = 1.

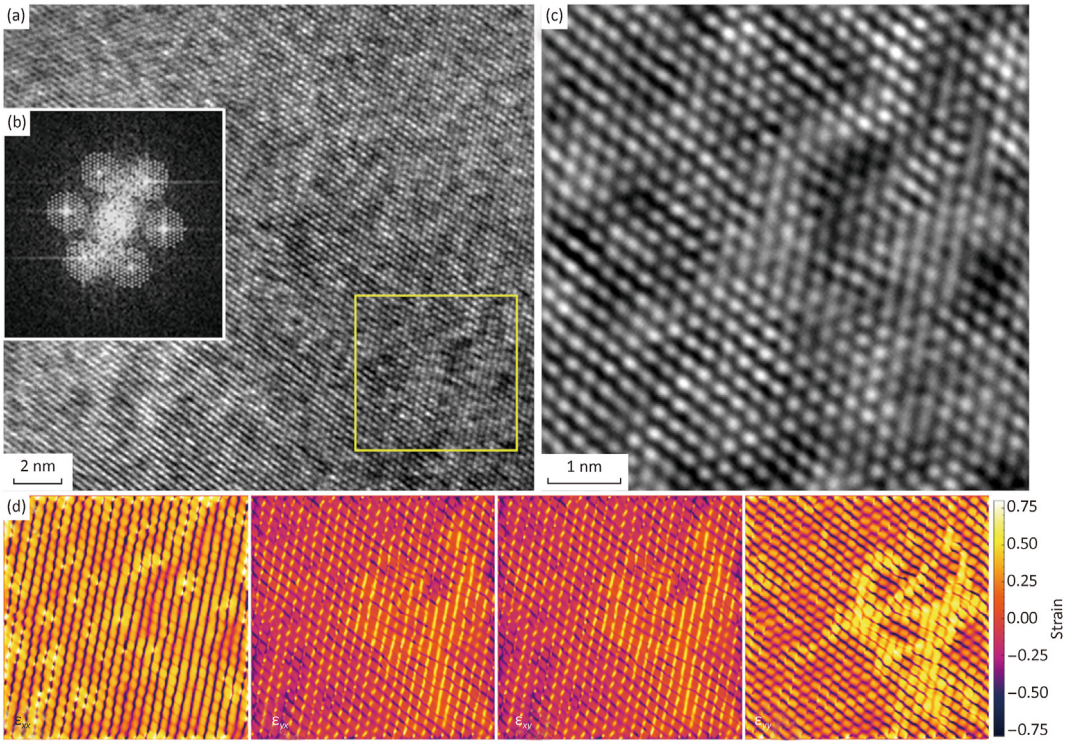

Fig. 10. (A) HR-TEM image of a HEB grain, zone axis [001], with (b) masked FFT of the yellow framed area, (c) resulting inverse FFT highlighting alteration to the crystal cell and (d) GPA maps showing strain accumulation corresponding to the defects.

distortions attributed to the incorporation of guest atoms and with formation of clusters or coherent precipitates, as the crystal planes are locally bent to be at the Braggs' condition [40,41]. Strain field maps were produced by applying the non-colinear Fourier

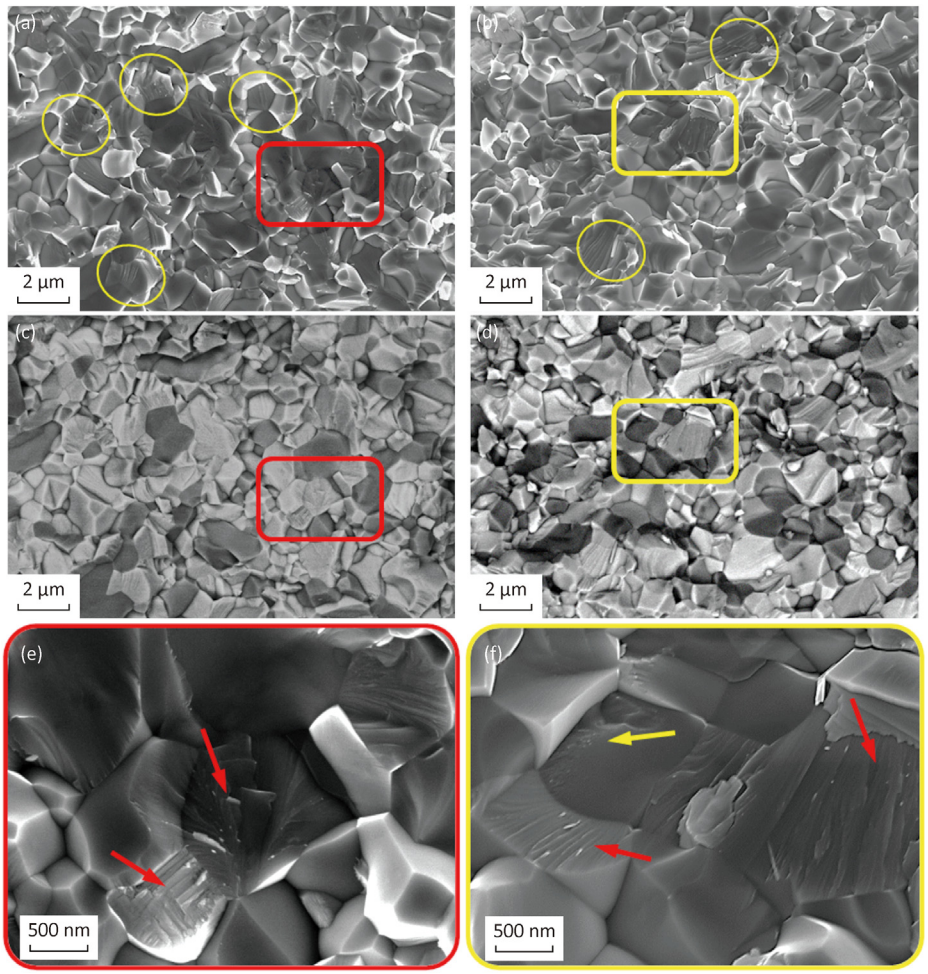

Fig. 11. SEM images recorded by (a), (b) In-lens and (c), (d) BSE showing the fracture mode in the dual ceramic. Note the zig-zag fracture and presence of bright particles in the magnified images in (e), (f). Red marks refer to HEC phase and yellow ones to HEB phase.

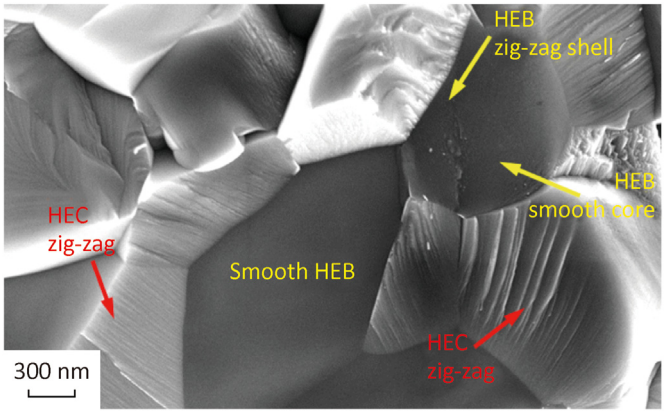

Fig. 12. Fracture surface showing different morphology in HEB and HEC grains.

component method which revealed 2D dimensional displacement fields [42] that were associated with compositional disorder, Fig. 9.

The high resolution TEM image in Fig. 10 shows how the solid solution affected the crystal lattice of the HEB grain. On average, the cell parameters of the crystal confirm what was observed by XRD analysis. The HEB has the *P*6/*mmm* structure while the HEC has the $Fm\bar{3}m$ structure, which correspond to the single metal boride and carbide phases. The lattice cell parameters of the HEB and HEC are the same as those obtained from a weighted average of the parameters of the single metal compounds predicted using the nominal concentrations of the metals present in each solid solution. However, HR-imaging highlighted how the crystal lattice locally contracted or expanded to accommodate smaller or larger metals, as evidenced by local compositional gradients. As a consequence, residual strains are present, as shown in the geometric phase analysis (GPA) maps produced using the software Strain++, Fig. 10d.

The predominant fracture mode was transgranular. The fracture surface shown in Fig. 11 was recorded with different imaging configurations to highlight the phase composition (BSE) and fine morphological features (In-lens). Carbide grains exhibited a peculiar transgranular zig-zag fracture path and prominent shear bands, as indicated with red boxes in Fig. 11. The surfaces of boride grains, indicated in yellow in Fig. 11, exhibited smoother fracture surfaces. Facets form on low index planes to minimize the surface energy, causing a slight increase in surface area, but if the energy on the planes is lower, then the overall energy can decrease and fracture is favored [43]. The energy for formation of facets on boride grains does not appear to be favorable compared to a flat surface across a random plane. The difference in the fracture mode between borides and carbides may be then related to energy differences between a random direction and the low-index planes, which is higher in the

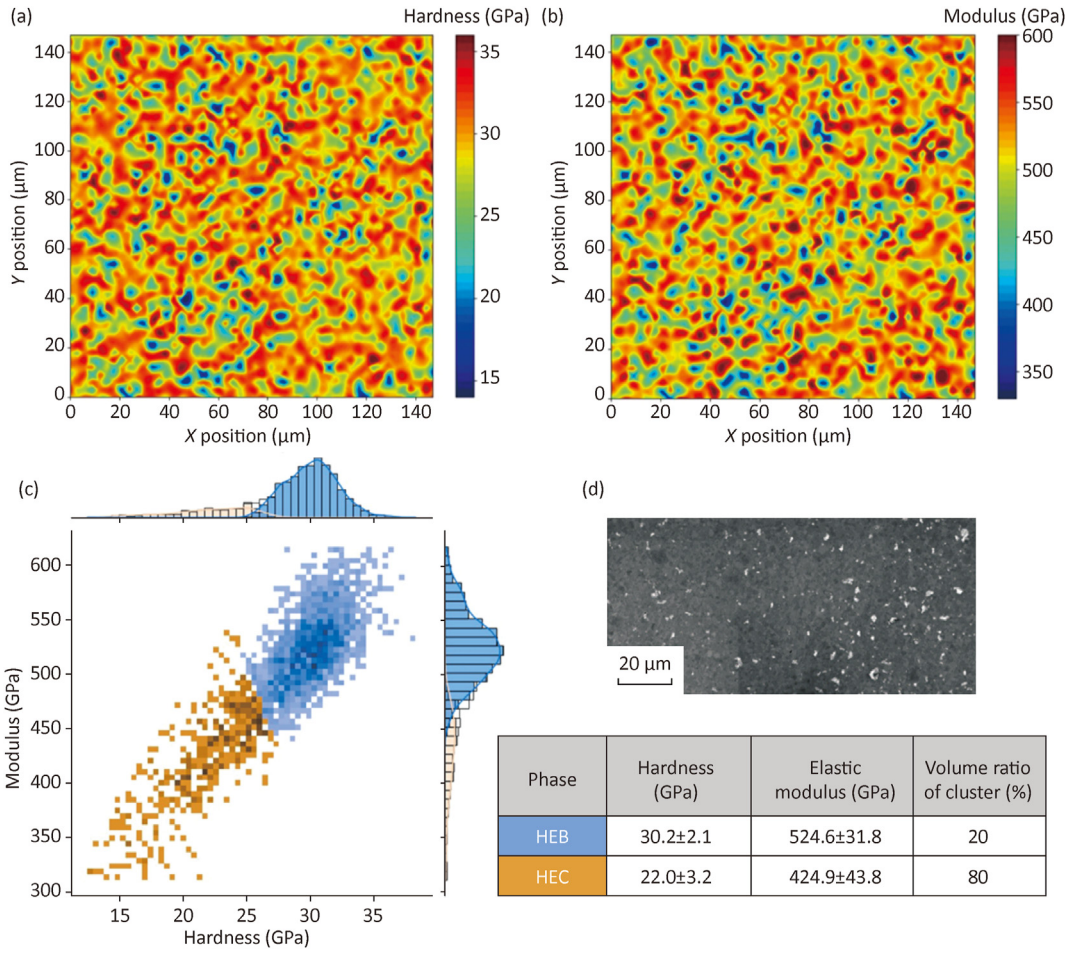

Phase	Hardness (GPa)	Elastic modulus (GPa)	Volume ratio of cluster (%)
HEB	30.2±2.1	524.6±31.8	20
HEC	22.0±3.2	424.9±43.8	80

Fig. 13. Contour plots of (a) hardness and (b) elastic modulus of the HEB-HEC ceramic under 5 mN load with (c) corresponding histograms deconvoluted into 2 major phases and (d) microstructure of the ceramic highlighting the distribution of the oxide phase, presumably associated to the lowest values of hardness and modulusreported in the table inset.

carbides than in the borides. Brighter nanosized particles were observed between the cleavage planes. Furthermore, in the boride grains, only the outer region of the grain displayed these characteristics, leaving the center flat and smooth, Figs. 11f and 12. This type of nano-patterned fracture in other simpler UHTC materials was ascribed to the presence of periodic defect structures and nanoinclusions in the shell region [22,44], which is consistent with the morphological structures described above.

3.2. Nanoindentation

The nanoindentation results are mapped in Fig. 13a and b. Both hardness and elastic modulus contour plots show the presence of a harder phase, around 30–35 GPa, represented by red and yellow, and a softer one, around 25 GPa, represented by green. According to previous investigations on dual high entropy materials [45–48], the harder phase should be the HEB and the softer phase the HEC. A much softer phase with hardness and modulus values around 16 GPa and 350 GPa, respectively, can be distinguished in blue coloring and, looking at the microstructural features reported for reference in Fig. 13d, it could be ascribed to the scattered $(Zr,Hf)O_2$ grains [49].

The indentation results were deconvoluted in two groups of data that estimated that the final material was composed of about 20% (in volume) of the harder HEB, and 80% of the softer HEC, Fig. 13c. These fractions differ from the designed proportions of the dual phase ceramic, 30% boride and 70% carbide. Indeed, none of the indentation data were discarded in this statistical study and, therefore, the higher fraction of softer phase also includes the scattered $(Zr,Hf)O_2$ particles, any local porosity upon grain pullout during polishing, and grain boundaries, which have been reported to have lower hardness than the grains [45].

Overall, the elastic moduli of the two main phases were ~525 GPa for the HEB and ~425 GPa for the HEC. These values are consistent with data reported in previous studies [45–47]. However, the hardness of the HEC measured in the present study was 22 GPa, which is notably lower than the previously reported value of 37 GPa [45]. Besides the reasons discussed above, the microstructural studies demonstrated preferential segregation of Hf and Ta to the carbide, which reduces the hardness of the HEC. The hardness values for single carbides are ~25 GPa for HfC and ~14 GPa for TaC [46], which are both lower than ~31 GPa reported for TiC [46]. Hence, the lower hardness of the HEC can be attributed also to Ti depletion from carbide grains.

3.3. Significance of investigations at the nanoscale

This section aims at making a connection between the nanoscale observations performed by HR-TEM and the local mechanical properties measured by nanoindentation. Previous literature lacks in exhibiting both properties and microstructural features at such length. Table 3 collects hardness values measured by

Table 3
Overview of HEB, HEC and dual phase HE materials with reported micro/nano-hardness. Fully dense ceramics are considered unless when specified. Compositions presented in this paper are marked with "pw".

Typology	Composition	Hardness (GPa)	Load (mN)	Note	Ref.
Dual	$(Ti,Zr,Hf,Nb,Ta)B_2$	30.2 ± 2.1	5	nano + HRTEM	pw
	(Ti,Zr,Hf,Nb,Ta)C	22.0 ± 3.2	5		pw [52]
	30HEB - 70HEC	26.5 ± 1.4	0.2 kg		
	$(Ti,Zr,Hf,Nb,Ta)B_2$	43.0 ± 2.9	~20	nano + HRTEM	[45,53]
	(Ti,Zr,Hf,Nb,Ta)C	37.4 ± 2.3	~20		
	30HEB - 70HEC	29.4 ± 2.0	1 kg		
	$(Ti,Zr,Hf,Nb,Ta)B_2$	21.3 ± 0.6	0.2 kg	HV	[24]
	80HEB - 20HEC	21.8 ± 0.8			
	60HEB - 40HEC	23.6 ± 0.3			
	40HEB - 60HEC	23.7 ± 0.6			
	20HEB - 80HEC (Ti,Zr,Hf,Nb,Ta)C	24.2 ± 0.3			
		23.1 ± 0.3			
HEC	(Ti,Zr,Hf,Nb,Ta)C	38.5 ± 0.5	~50	nano	[54]
	(Ti,Zr,Hf,Nb,Ta)C	40.6 ± 0.6	8	nano	[55]
	(Ti,Zr,Hf,Ta,W)C	//	50–500	data not reported	[56]
	(V,Nb,Ta,Mo,W)C				
	(Ti,Zr,Hf,Nb,Ta)C	33.4 ± 1.1	2	nano/HV	[57]
	(Ti,Zr,Hf,Ta,Cr)C	23.5 ± 2.3	0.2 kg		
	(Ti,Zr,Hf,Ta,W)C	~27	0.2 kg		
	(Ti,Zr,Hf,Ta,Mo)C	35.1 ± 1.8	2		
	(Ti,Zr,Hf,Mo,W)C	27.1 ± 2.0	0.2 kg		
		~29	0.2 kg		
		43.4 ± 2.9	2		
		29.0 ± 0.9	0.2 kg		
	(Ti,Zr,Nb,Ta,Mo)C	31.3 ± 2.5	100	nano/HV	[58]
		25.3 ± 0.3	1 kg		
HEB	$(Ti,Zr,Hf,Nb,Ta)B_2$	17.5 ± 1.2	0.2 kg	density ~92%;	[4]
	$(Ti,Zr,Hf,Ta,Mo)B_2$	19.1 ± 1.8		ind. width: 20–25 μm	
	$(Ti,Zr,Hf,Nb,Mo)B_2$	21.9 ± 1.7		HV + HRTEM	
	$(Ti,Hf,Nb,Ta,Mo)B_2$	22.5 ± 1.7			
	$(Ti,Zr,Nb,Ta,Mo)B_2$	23.7 ± 1.7			
	$(Ti,Zr,Nb,Ta,Cr)B_2$	19.9 ± 2.6			
	$(Ti,Zr,Hf,Ta,Cr)B_2$	28.3 ± 1.6	0.2 kg	HV	[59]
	$(Ti,Zr,Hf,Nb,Mo)B_2$	26.3 ± 0.7			
	$(Ti,Hf,Nb,Ta,Mo)B_2$	25.9 ± 1.1			
	$(Ti,Zr,Hf,Nb,Ta)B_2$	16.4 ± 0.5	0.2 kg	HV	[60]
	$(Ti,Zr,Hf,Mo,W)B_2$	27.7 ± 1.1			
	$(Ti,Zr,Hf,Nb,Ta)B_2$	20.5 ± 1.0	0.2 kg	HV	[61]

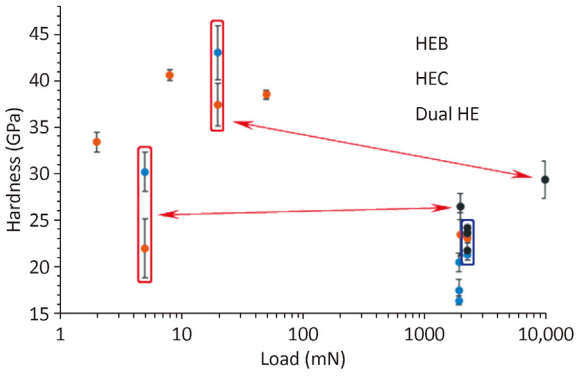

Fig. 14. Selection of nano- and micro-hardness values performed on HEB, HEC and dual phase HE ceramics containing Ti, Zr, Hf, Nb, and Ta, see Table 3. Circled and connected data in red refer to the same material [45,52], circled data in blue derive from the same research group [24].

nanoindentation or Vickers hardness on HEB, HEC and dual phase high entropy ceramics with variable composition.

It is immediately noticeable that, given the countless composition possibilities, in terms of cations included in the boride or carbide, of the variable microstructural features deriving from the processing (density, grain size, segregation, precipitation), and even in terms of relative amount of boride and carbide in the dual phase ceramics, making direct comparison is a hard task. However, keeping fixed the 5 main cations, Ti,Zr,Hf,Nb,Ta, the plot in Fig. 14 provides some indications.

Besides the present work, the local properties of individual HEB and HEC were only considered in Ref. [45], which found that the borides were harder than carbides for the reasons given in the previous paragraph, *i.e.* related to a depletion of the metal that formed the hardest compounds, Ti. Here, Zr-rich nanoinclusions were found in the HEB grains and Ti-rich nanoinclusons were found in HEC grains. The nanoinclusions produced strained regions in the boride phase, which also contained more dislocation networks as compared to the carbide, Figs. 7 and 10. The presence of the strained regions is related to the nature of the hexagonal structure of the HEB, which is more densely packed than the cubic structure of the HEC. The combination of these features contributed to the increased hardness of the HEB grains as compared to HEC ones.

The question whether the dual phase high entropy ceramic is harder than the constituent HEBs or HECs phases remains unsolved

at present. To date, only one experimental work compares the hardness of HEB, HEC and several dual HEB-HEC composites [24], but since 0.2 kg load was used, resulting in indents as wide as 20–25 μm [4], the results are too much dependent on the overall microstructural features.

One aspect that deserves further investigation is the possibility of producing nanostructures -nanoinclusions and dislocation tangles-within micron-sized grains. Similar features can further enhance the hardness in some high-entropy materials, such as ultra-hard carbon-doped high entropy alloys [50], or in high entropy carbides [51].

4. Conclusions

A dual phase ceramic containing Hf, Nb, Ta, Ti, and Zr was produced by reduction synthesis and densification by spark plasma sintering. The ceramic contained about 70% (in volume) carbide phase and about 30% boride phase.

SEM and TEM analysis highlighted the uneven distribution of metals between the two phases with Ti and Nb preferentially segregating to the boride, and Hf and Ta segregating to the carbide. The concentration of Zr was about the same between the two phases, possibly due to the processing route that introduced a higher quantity of Zr and blurred preferential segregation. Furthermore, each grain displayed a multi-shell structure with a gradient of metal concentration and nanosized inclusions. The nature of the inclusions (boride, carbide, metal, oxide) is not clear at present, but they are presumably the result of local miscibility gaps. Due to the distorted lattice, linear defects and strains accumulation were typical of both carbide and boride phases.

Nanoindentation under a force of 5 mN revealed that the boride had higher hardness, ~30 GPa, and modulus, ~525 GPa, compared to the carbide phase, which had a hardness of 22 GPa and modulus of 425 GPa. The property values for the multi-cation boride were comparable to previous reports. In contrast, the values measured for carbides in the present study were lower than previous reports possibly due to the enrichment of Ta and Hf in the carbide. The higher hardness of the HEB is presumably ascribed also to the more strained hexagonal structure as compared to the more compliant cubic structure of the HEC and to the presence of dislocation tangles.

Data availability

The raw and processed data required to reproduce these findings cannot be shared at this time due to legal or ethical reasons.

CRediT authorship contribution statement

Steven M. Smith: Investigation. **Nicola Gilli:** Investigation. **William G. Fahrenholtz:** Funding acquisition, Supervision, Writing – review & editing. **Gregory E. Hilmas:** Funding acquisition, Supervision, Writing – review & editing. **Sandra García-González:** Investigation. **Emilio Jiménez-Piqué:** Investigation, Funding acquisition. **Stefano Curtarolo:** Funding acquisition, Supervision, Writing – review & editing. **Laura Silvestroni:** Conceptualization, Formal analysis, Funding acquisition, Project administration, Supervision, Visualization, Writing – original draft, Data curation.

Declaration of competing interest

The authors declare that they have no known competing financial interests or personal relationships that could have appeared to influence the work reported in this paper.

Acknowledgements

This research was partially sponsored by the NATO Science for Peace and Security Programme under grant MYP-G5767 (SUSPENCE) and by the US AFOSR through the grant no. FA9550-21-1-0399 (NACREOUS). Part of the work was funded by the Spanish Science and Innovation Ministry though grant PID2021-126614OB-I00. Research at Missouri S&T was also supported by the Office of Naval Research through a Multidisciplinary University Research Initiative (MURI) program under project number N00014-21-1-2515.

References

[1] Akrami S, Edalati P, Fuji M, Edalati K. High-entropy ceramics: review of principles, production and applications. Mater Sci Eng R Rep 2021;146:100644.
[2] Yeh J-W, Chen S-K, Lin S-J, Gan J-Y, Chin T-S, Shun T-T, et al. Nanostructured high-entropy alloys with multiple principal elements: novel alloy design concepts and outcomes. Adv Eng Mater 2004;6:299–303.
[3] Rost CM, Sachet E, Borman T, Moballegh A, Dickey EC, Hou D, et al. Entropy-stabilized oxides. Nat Commun 2015;6:8485.
[4] Gild J, Zhang Y, Harrington T, Jiang S, Hu T, Quinn MC, Mellor WM, Zhou N, Vecchio K, Luo J. High-Entropy Metal Diborides: a new class of high-entropy materials and a new type of ultrahigh temperature ceramics. Sci Rep 2016;6:37946.
[5] Sarker P, Harrington T, Toher C, Oses C, Samiee M, Maria J-P, Brenner DW, Vecchio KS, Curtarolo S. High-entropy high-hardness metal marbides discovered by entropy descriptors. Nat Commun 2018;9:4980.
[6] Toher C, Oses C, Hicks D, Curtarolo S. Unavoidable disorder and entropy in multi-component systems. Computat. Mater. 2019;5:1.
[7] Oses C, Toher C, Curtarolo S. High-entropy ceramics. Nat Rev Mater 2020;5:295–309.
[8] Feng L, Fahrenholtz WG, Brenner DW. High-entropy ultra-high-temperature borides and carbides: a new class of materials for extreme environments. Annu Rev Mater Res 2021;51:165–85.
[9] Fahrenholtz WG, Wuchina EJ, Lee WE, Zhou Y. Ultra-high temperature ceramics: materials for extreme environment applications. Hoboken, New Jersey: John Wiley & Sons Inc; 2014.
[10] Dippo OF, Mesgarzadeh N, Harrington TJ, Schrader GD, Vecchio KS. Bulk high-entropy nitrides and carbonitrides. Sci Rep 2020;10:21288.
[11] Sarkar A, Velasco L, Wang D, Wang Q, Talasila G, de Biasi L, Kübel C, Brezesinski T, Bhattacharya SS, Hahn H, Breitung B. High entropy oxides for reversible energy storage. Nat Commun 2018;9:3400.
[12] Edalati P, Shen X-F, Watanabe M, Ishihara T, Arita M, Fuji M, Edalati K. High-entropy oxynitride as a low-bandgap and stable photocatalyst for hydrogen production. J Mater Chem A 2021;9:15076–86.
[13] Dube TC, Zhang J. Underpinning the relationship between synthesis and properties of high entropy ceramics: a comprehensive review on borides, carbides and oxides. J Eur Ceram Soc 2024;44:1335–50.
[14] Dusza J, Švec P, Girman V, Sedlák R, Castle EG, Csanádi T, Kovalčíková A, Reece MJ. Microstructure of (Hf-Ta-Zr-Nb)C high-entropy carbide at micro and nano/atomic level. J Eur Ceram Soc 2018;38:4303–7.
[15] Feng L, Fahrenholtz WG, Hilmas GE, Monteverde F. Effect of Nb content on the phase composition, densification, microstructure, and mechanical properties of high-entropy boride ceramics. J Eur Ceram Soc 2021;41:92–100.
[16] Feng L, Fahrenholtz WG, Hilmas GE. Processing of dense high-entropy boride ceramics. J Eur Ceram Soc 2020;40:3815–23.
[17] Ye YF, Wang Q, Lu J, Liu CT, Yang Y. High-entropy alloy: challenges and prospects. Mater Today 2016;19:349–62.
[18] Feng L, Chen WT, Fahrenholtz WG, Hilmas GE. Strength of single-phase high-entropy carbide ceramics up to 2300°C. J Am Ceram Soc 2021;104:419–27.
[19] Liu J, Yang Q-Q, Zou J, Wang W-M, Wang X-G, Fu Z-Y. Strong high-entropy diboride ceramics with oxide impurities at 1800°C. Sci China Mater 2023;66:2061–70.
[20] Feng L, Fahrenholtz WG, Hilmas GE, Zhou Y, Bai J. Strength retention of single-phase high-entropy diboride ceramics up to 2000°C. J Am Ceram Soc 2024;107:1895–904.
[21] Silvestroni L, Kleebe H-J, Fahrenholtz WG, Watts J. Super-strong materials for temperatures exceeding 2000 °C. Sci Rep 2017;7:40730.
[22] Gilli N, Watts J, Fahrenholtz WG, Sciti D, Silvestroni L. Design of ultra-high temperature ceramic nano-composites from multi-scale length microstructure approach. Comput Bus 2021;226:109344.
[23] Fu Z, Jiang L, Wardini JL, MacDonald BE, Wen H, Xiong W, Zhang D, Zhou Y, Rupert TJ, Chen W, Lavernia EJ. A high-entropy alloy with hierarchical nanoprecipitates and ultrahigh strength. Sci Adv 2018;4:eaat8712.
[24] Luo SC, Guo WM, Plucknett K, Lin H-T. Fine-grained dual-phase high-entropy ceramics derived from boro/carbothermal reduction. J Eur Ceram Soc 2021;41:3189–95.
[25] Smith SM, Fahrenholtz WG, Hilmas GE, Huang T. Pressureless sintering of

dual-phase, high-entropy boride–carbide ceramics. J Am Ceram Soc 2023;106:3359–63.
[26] Huo S, Chen L, Liu X, Kong Q, Wang Y, Gu H, Zhou Y. Reactive sintering of dual-phase high-entropy ceramics with superior mechanical properties. J Mater Sci Technol 2022;129:223–7.
[27] Naughton-Duszová A, Švec P, Kovalčíková A, Sedlák R, Tatarko P, Hvizdoš P, Šajgalík P, Dusza J. On the phase and grain boundaries in dual phase carbide/boride ceramics from micro to atomic level. J Eur Ceram Soc 2023;43:6765–73.
[28] Qin M, Gild J, Hu C, Wang H, Hoque MSB, Braun JL, Harrington TJ, Hopkins PE, Vecchio KS, Luo J. Dual-phase high-entropy ultra-high temperature ceramics. J Eur Ceram Soc 2020;40:5037–50.
[29] Feng L, Fahrenholtz WG, Hilmas GE, Curtarolo S. Boro/carbothermal reduction co-synthesis of dual-phase high-entropy boride-carbide ceramics. J Eur Ceram Soc 2023;43:2708–12.
[30] Smith SM, M Fahrenholtz WG, Hilmas GE, Curtarolo S. Thermodynamic analysis of metal segregation in dual phase high entropy ceramics. J Mater 2024;10:889–95.
[31] Smith SM, Feng L, Fahrenholtz WG, Hilmas GE, Huang T. High-entropy boride–carbide ceramics by sequential boro/carbothermal synthesis. J Am Ceram Soc 2022;105:5543–7.
[32] Oliver WC, Pharr GM. An improved technique for determining hardness and elastic modulus using load and displacement sensing indentation experiments. J Mater Res 1992;7:1564–82.
[33] Wang Y-P, Gan G-Y, Wang W, Yang Y, Tang B-Y. Ab initio prediction of mechanical and electronic properties of ultrahigh-temperature high-entropy ceramics ($Hf_{0.2}Zr_{0.2}Ta_{0.2}M_{0.2}Ti_{0.2})B_2$ (M = Nb, Mo, Cr). Phys Status Solidi B 2018;255:1800011.
[34] Silvestroni L, Sciti D. Transmission electron microscopy on Hf- and Ta-carbides sintered with $TaSi_2$. J Eur Ceram Soc 2011;31:3033–43.
[35] Ohtaki K, Patel M, Crespillo M, Karandikar K, Yanwen Z, Graeve O, Mecartney M. Improved high temperature radiation damage tolerance in a three-phase ceramic with heterointerfaces. Sci Rep 2018;8:13993.
[36] Maldonado AJ, Misra KP, Misra RDK. Grain boundary segregation in a high entropy alloy. Mater Technol 2023;38:2221959.
[37] Dai F-Z, Wen B, Sun Y, Ren Y, Xiang H, Zhou Y. Grain boundary segregation induced strong UHTCs at elevated temperatures: a universal mechanism from conventional UHTCs to high entropy UHTCs. J Mater Sci Technol 2022;123:26–33.
[38] Wang C, Qin M, Lei T, He Y, Kisslinger K, Rupert TJ, Luo J, Xin HL. Synergic grain boundary segregation and precipitation in W- and W-Mo-containing high-entropy borides. J Eur Ceram Soc 2021;41:5380–7.
[39] Tang X, Thompson GB, Ma K, Weinberger CR. The role of entropy and enthalpy in high entropy carbides. Comput Mater Sci 2022;210:111474.
[40] Raghavendra RM, Divya Iyer G, Kumar A, Subramaniam A. Surface stress mediated image force and torque on an edge dislocation. Phil Mag 2018;98:1731–43.
[41] Wu M, Trampert A. Coherent GdN clusters in epitaxial GaN:Gd thin films determined by transmission electron microscopy. Nanotechnology 2013;24:255701.
[42] Hÿtch MJ, Snoeck E, Kilaas R. Quantitative measurement of displacement and strain fields from HREM micrographs. Ultramicroscopy 1998;74:131–46.
[43] Wang S, Liu G, Wang L. Crystal facet engineering of photoelectrodes for photoelectrochemical water splitting. Chem Rev 2019;119:5192–247.
[44] Silvestroni L, Gilli N, Migliori A, Scit D, Watts J, Hilmas GE, Fahrenholtz WG. A simple route to fabricate strong boride hierarchical composites for use at ultra-high temperature. Comput Bus 2020;183:107618.
[45] Naughton Duszová A, Ďaková L, Csanádi T, Kovalčíková A, Kombamuthu V, Ünsal H, Tatarko P, Tatarková M, Hvizdoš P, Šajgalík P. Nanohardness and indentation fracture resistance of dual-phase high-entropy ceramic. Ceram Int 2023;49:24239–45.
[46] Harrington TJ, Gild J, Sarker P, Toher C, Rost CM, Dippo OF, McElfresh C, Kaufmann K, Marin E, Borowski L, Hopkins PE, Luo J, Curtarolo S, Brenner DW, Vecchio KS. Phase stability and mechanical properties of novel high entropy transition metal carbides. Acta Mater 2019;166:271–80.
[47] Castle E, Csanádi T, Grasso S, Dusza J, Reece M. Processing and properties of high-entropy ultra-high temperature carbides. Sci Rep 2018;8:8609.
[48] Liu J-X, Shen X-Q, Wu Y, Li F, Liang Y, Zhang G-J. Mechanical properties of hot-pressed high-entropy diboride-based ceramics. J Adv Ceram 2020;9:503–10.
[49] Aboushahba M, Katamish H, Elagroudy M. Evaluation of hardness and wear of surface treated zirconia on enamel wear. An in-Vitro Study. Future Dental J. 2018;4:76–83.
[50] Edalati P, Mohammadi A, Tang Y, Floriano R, Fuji M, Edalati K. Phase transformation and microstructure evolution in ultrahard carbon-doped AlTiFeCoNi high-entropy alloy by high-pressure torsion. Mater Lett 2021;302:130368.
[51] Hu J, Yang Q, Zhu S, Zhang Y, Yan D, Gan K, Li Z. Superhard bulk high-entropy carbides with enhanced toughness *via* metastable *in-situ* particles. Nat Commun 2023;14:5717.
[52] Smith SM, Feng L, Fahrenholtz WG, Hilmas GE, Huang T. High-entropy boride–carbide ceramics by sequential boro/carbothermal synthesis. J Am Ceram Soc 2022;105:5543–7.
[53] Naughton-Duszová A, Medveď D, Ďaková L, Kovalčíková A, Švec P, Tatarko P, Ünsal H, Hvizdoš P, Šajgalík P, Dusza J. Dual-phase high-entropy carbide/boride ceramics with excellent tribological Properties. J Eur Ceram Soc 2024;44:5391–400.
[54] Dusza J, Csanádi T, Medveď D, Sedlák R, Vojtko M, Ivor M, Ünsal H, Tatarko P, Tatarková M, Šajgalík P. Nanoindentation and tribology of a (Hf-Ta-Zr-Nb-Ti)C high-entropy carbide. J Eur Ceram Soc 2021;41:5417–26.
[55] Ye B, Wen T, Huang K, Wang C-Z, Chu Y. First-principles study, fabrication, and characterization of $(Hf_{0.2}Zr_{0.2}Ta_{0.2}Nb_{0.2}Ti_{0.2})C$ high-entropy ceramic. J Am Ceram Soc 2019;102:4344–52.
[56] Sangiovanni DG, Mellor W, Harrington T, Kaufmann K, Vecchio K. Enhancing plasticity in high-entropy refractory ceramics *via* tailoring valence electron concentration. Mater Des 2021;209:109932.
[57] Brune PM, Hilmas GE, Fahrenholtz WG, Watts JL, Ryan CJ, DeSalle CM, Wolfe DE, Curtarolo S. Hardness of single phase high entropy carbide ceramics with different Compositions. J Appl Phys 2024;135:165106.
[58] Wang K, Chen L, Xu C, Zhang W, Liu Z, Wang Y, Ouyang J, Zhang X, Fu Y, Yu Zhou Y. Microstructure and mechanical properties of (TiZrNbTaMo)C high-entropy ceramic. J Mater Sci Technol 2020;39:99–105.
[59] Zhang Y, Guo W-M, Jiang Z-B, Zhu Q-Q, Sun S-K, You Y, Plucknett K, Lin H-T. Dense high-entropy boride veramics with ultra-high hardness. Scripta Mater 2019;164:135–9.
[60] Zhang Y, Sun S-K, Zhang W, You Y, Guo W-M, Chen Z-W, Yuan J-H, Lin H-T. Improved densification and hardness of high-entropy diboride ceramics from fine powders synthesized *via* borothermal reduction process. Ceram Int 2020;46:14299–303.
[61] Gild J, Wright A, Quiambao-Tomko K, Qin M, Tomko JA, Shafkat bin Hoque M, Braun JL, Bloomfield B, Martinez D, Harrington T, Vecchio K, Hopkins PE, Luo J. Thermal conductivity and hardness of three single-phase high-entropy metal diborides fabricated by borocarbothermal reduction and spark plasma sintering. Ceram Int 2020;46:6906–13.

Steven M. Smith is a Ceramic Engineering Ph.D. candidate at Missouri University of Science and Technology in the Department of Materials Science and Engineering. He received a B.S. degree in Ceramic Engineering from the Missouri University of Science and Technology in 2021 and began his Ph.D. the same year. His current research includes synthesis and densification of ultra-high temperature ceramics including high-entropy borides, carbides, and dual-phase ceramics.

Laura Silvestroni is a senior researcher at CNR-ISSMC (former CNR-ISTEC). She received her M.S. degree in Products, Materials, and Processes for the Industrial Chemistry and Ph.D. degree in Industrial Chemistry from the University of Bologna, Italy. Her field of expertise includes the design, processing, and characterization of structural ceramics and composites, with an emphasis on materials for severe environments. She is lead author or co-author of about 140 papers and Editor of the *Journal of the European Ceramic Society*. She is principal investigator (PI) and co-PI of grants funded by national and international government agencies and companies.